




Scale-independent model based on fractal theory for calculating the adhesion force between a particle and rough surfaces

Xiao Wang ¹, Weidong Wang ^{1,*}, Yingmin Zhu,¹ Ji Zhang ^{1,†} and Haiyan Zhang^{1,2,‡}

¹*School of Mechano-Electronic Engineering, Xidian University, Xi'an 710071, People's Republic of China*

²*Science and Technology on Vacuum Technology and Physics Laboratory, Lanzhou 730000, People's Republic of China*



(Received 3 May 2024; accepted 20 August 2024; published 12 September 2024)

The elimination of the scale-dependent statistical parameters is a challenge in the estimation of the van der Waals force between a particle and rough surfaces. Herein, a scale-independent parameter, the fractal dimension, was introduced into the Rabinovich model to calculate the microadhesion force. First, a Weierstrass-Mandelbrot function is proposed to generate a random 2D contour, which has a simplified form and is more reasonable for spectrum analysis. And then, the roughness scale extraction method was employed to calculate the fractal-dimension value of the real aluminum (Al) surface. And last, the proposed scale-independent Rabinovich-Fractal model was used to calculate the adhesion forces, which are consistent with the results of the atomic force microscopy adhesion test. Aside from providing a more accurate estimation of the van der Waals forces, the proposed model is not influenced by the sampling scale of the surface roughness measurement, which eliminates the related error in van der Waals force estimation.

DOI: [10.1103/PhysRevE.110.034802](https://doi.org/10.1103/PhysRevE.110.034802)

I. INTRODUCTION

At the micro- and nanoscale, weak interaction is crucial. It facilitates bonding between micro- and nanodevices and enables the manipulation of micro- and nanorobots. Therefore, analyzing the microscopic forces on microscale interfaces and surfaces is particularly important [1–5]. In the field of surface and interface analysis, an accurate assessment of topography is critical, in particular because the surface quality is often evaluated using parameters such as surface roughness. However, traditional metrics such as roughness are subject to variations caused by the measurement scale and instrument resolution, resulting in inconsistent estimation of van der Waals force at different scales [6–8]. This inconsistency highlights the need for a scale-independent parameter to characterize rough surfaces effectively. Fractal theory addresses this need by providing a more accurate analysis than roughness at the microscale. It is less affected by the measurement resolution and provides a more objective and reliable assessment of surface characteristics such as complexity, irregularity, and space-filling capacity [9,10]. The essence of the fractal theory is the fractal dimension (D), a key parameter that captures the complex inherent in fractal objects. The value of D , which typically ranges between 1 and 2 for line profiles and 2 and 3 for 3D surface topography, indicates the irregularity and degree of fragmentation of the surface. Crucially, the value of D is independent of the measuring scale within certain limits.

Assessing the fractal dimension accurately is key to realizing a scale-independent evaluation of the surface and interface. Various methods have been developed to calculate the value of D , each with its unique principles and applications. These methods can be broadly classified as scale and spectrum methods. As a typical representative scale method, the box-counting method is widely used for surface evaluation even with its low accuracy [11–13]. The spectrum method consists of many specific ways, such as the power spectral density (PSD) method [14,15], structure function (SF) method [16,17], and roughness scaling extraction (RSE) method [18,19]. These are all based on the spectrum analysis or closely related spectrum. Each method exhibits different accuracies and is suitable for specific applications.

Combining fractal theory with the contact mechanism is a method that can simplify surface statistical measurements. As early as 1990, Majumdar and Bhushan [20] introduced fractal theory into contact mechanism to predict elastic and plastic contacts. At the same time, the contact theory based on fractal theory suggests that it is a scale-independent method [21]. With the development of micro-(nano) technology, microscale contacts have attracted increasing attention, and the contact between microrough surfaces has become an important topic of study. However, the scale-dependent parameter still limits the application of rough surface contacts, such as the Greenwood-Williamson [22], Greenwood-Tripp [23], and Rabinovich [24] models. All of these predict the contact force through statistical parameters that are sensitive to scale of the measurement.

In this study, to realize the scale-independent rough surfaces adhesion force measurements, the fractal dimension was introduced into the Rabinovich [25] model to propose a model where the adhesion force only depends on the value of D

*Contact author: wangwd@mail.xidian.edu.cn

†Contact author: zhangji@xidian.edu.cn

‡Contact author: zhy_zhanghaiyan@163.com

and scaling length L . First, a more reasonable form of the Weierstrass-Mandelbrot function was proposed to simulate the true 2D contours. Then, the roughness scaling extraction (RSE) method was chosen as the way to calculate fractal dimension, which has the best accuracy among the three methods. Finally, the fractional dimension D was introduced into the Rabinovich model to replace the original rms and obtain the Rabinovich fractal (RF) model, which is validated by the atomic force microscope (AFM) adhesion force experiment. In addition, the dynamic contact process was observed by an *in situ* scanning electron microscope (SEM) observation system [26,27].

II. MATERIALS AND METHODS

A. Surface type

Two surface types were used in this study: an artificial surface profile and an actual etched-aluminum (Al) rough surface. The artificial surface profile was generated by the WM function.

The WM function is a mathematical example of a continuous yet nowhere differentiable real-valued function. This function exhibits fractal characteristics and is commonly employed in the simulation of fractal contours. The original form of the WM [28] function is given by Eq. (1):

$$W(t) = \sum_{n=-\infty}^{\infty} \frac{(1 - e^{j\gamma^n t})e^{j\phi_n}}{\gamma^{(2-D)n}} \quad (1 < D < 2, \gamma > 1, \phi_n: \text{arbitrary phases}), \quad (1)$$

where D is the fractal dimension. γ is a parameter related to frequency, and ϕ_n represent a series of random phases to make $W(t)$ exhibit stochastic behavior. Because of the ϕ_n , $W(t)$ is a random process.

The physical significance of the WM function lies in its ability to model complex, irregular shapes that are prevalent in nature. By adjusting parameters γ and D , the function can accurately mimic the statistical properties of various natural fractals.

To ensure confidence in the profile description, the profile height must be a real number. The real part of a complex random process was selected to generate the profile data. To make the analysis easier, it was assumed that ϕ_n obeys a uniform distribution in $[0, 2\pi]$. To simplify the understanding, variable t was replaced with x as shown in the following equation, which represents the location of the coordinates of the height data:

$$Z(x) = \text{Re}W(x) = \sum_{n=-\infty}^{\infty} \frac{\cos \phi_n - \cos(\gamma^n x + \phi_n)}{\gamma^{(2-D)n}} \quad [1 < D < 2, \gamma > 1, \phi_n \sim U(0, 2\pi)]. \quad (2)$$

To examine the stationarity of the random process $Z(x)$, the expectation ($E[*]$) and the autocorrelation function (ACF) are calculated by Eqs. (3) and (4) as follows:

$$E[Z(x)] = \sum_{n=-\infty}^{\infty} E \left[\frac{\cos \phi_n - \cos(\gamma^n x + \phi_n)}{\gamma^{(2-D)n}} \right] = 0 \quad (3)$$

$$E[Z(x + \tau)Z(x)] = \sum_{n=-\infty}^{\infty} \frac{1 + \cos \gamma^n \tau - \cos \gamma^n x - \cos \gamma^n (\tau + x)}{2\gamma^{(4-2D)n}} \quad (4)$$

From Eqs. (3) and (4), ACF is not only related to the distance τ between two locations, but also to the starting location x_s of the state, even though the expectation is a constant of 0, so $Z(x)$ is not a wide stationary stochastic process. Therefore, it is more appropriate to use it to model the fractal contours in nature, because most of the surface profiles in nature are a nonstationary stochastic process [29].

To use a function to simulate an actual fractal profile, it must have fractal characteristics and describe a stochastic process. As mentioned previously, it is most reasonable to use Eq. (2); however, for nonstationary stochastic processes, very few analytical tools exist to achieve a deep analysis of the function. Therefore, to be able to analyze it better in the frequency domain, we restrict that the function be a wide stationary stochastic process, which may decrease accuracy in simulating the real surface, but still retains the stochasticity of the process and the fractal characteristics. Thus, using wide stationary stochastic processes to simulate the true surface profiles is acceptable to some extent. Therefore, Eq. (2) is simplified as Eq. (5):

$$h(x) = \sum_{n=-\infty}^{\infty} \frac{\cos(\gamma^n x + \phi_n)}{\gamma^{(2-D)n}} \quad [1 < D < 2, \gamma > 1, \phi_n \sim U(0, 2\pi)], \quad (5)$$

$$E[h(x)] = \sum_{n=-\infty}^{\infty} E \left[\frac{\cos(\gamma^n x + \phi_n)}{\gamma^{(2-D)n}} \right] = 0, \quad (6)$$

$$E[h(x + \tau)h(x)] = E \left[\sum_{m=-\infty}^{\infty} \sum_{n=-\infty}^{\infty} \frac{\cos(\gamma^m (x + \tau) + \phi_m)}{\gamma^{(2-D)m}} \frac{\cos(\gamma^n x + \phi_n)}{\gamma^{(2-D)n}} \right] = \sum_{n=-\infty}^{\infty} \frac{\cos \gamma^n \tau}{\gamma^{(4-2D)n}} \quad (7)$$

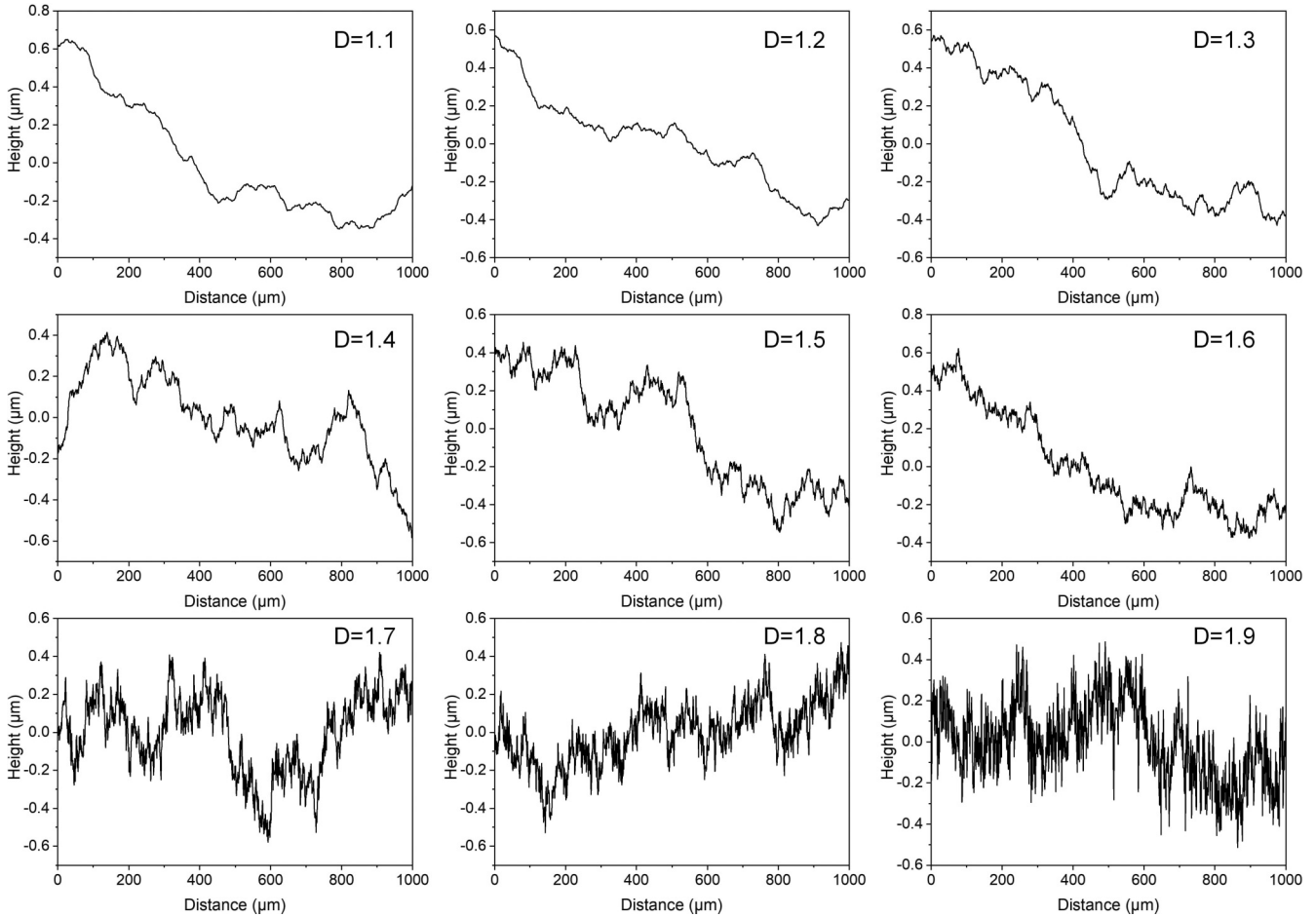


FIG. 1. Artificial 2D contour generated by WM function $h(x)$ with ideal fractal-dimension values ranging from 1.1 to 1.9.

Equations (6) and (7) shows that the expectation of $h(x)$ is a constant of 0, and the ACF is related only to the distance τ between the two locations, and is not related to the starting location. Therefore, $h(x)$ represents a wide stationary stochastic process. The calculation of the fractal dimension (D_c) of the simulated contours was performed in this study on the basis of $h(x)$.

As shown in Fig. 1, a group of 2D contours with different fractal dimensions using $h(x)$ has been generated. One thousand data points were generated over a distance of 1 mm. The complexity of the 2D contours increased as the ideal fractal dimension (D_i) increased.

The etched Al surface was prepared using chemical and electrochemical methods, as described in our previous study [30]. The topographic data were obtained using AFM (MFP-3D, AR) with an AC240TS tip. The curvature of the tip was approximately 10 nm, the scanning model was set as air, and two types of regions (20×20 and $5 \times 5 \mu\text{m}^2$) were selected for the data acquisition.

B. Fractal-dimension calculation methods

1. Power spectrum density

According to the Wiener-Khinchin theorem [31], the power spectrum is the Fourier transform of the ACF of a wide

stationary stochastic process. The power spectrum can be obtained by

$$G_h(\omega) = \int_{-\infty}^{\infty} R_h(\tau) e^{-j\omega\tau} d\tau = \sum_{n=0}^{\infty} \frac{\pi \delta(\omega - \gamma^n)}{2\gamma^{(4-2D)n}}, \quad (8)$$

where δ represents the Dirichlet function. According to Berry's method [28], Eq. (8) has a continuous form:

$$\overline{G}_h(\omega) = \frac{\pi}{2 \ln \gamma} \frac{1}{\omega^{(5-2D)}}. \quad (9)$$

Equation (9) shows that $\overline{G}_h(\omega) \propto \omega^{2D-5}$; thus, the value of D can be easily obtained from the log-log fitting results.

2. Structure function

The SF method is an improved version of ACF, which is proposed as shown as $F(\tau)$ in Eq. (11):

$$R_h(\tau) = E[h(x + \tau)h(x)] = \sum_{n=-\infty}^{\infty} \frac{\cos \gamma^n \tau}{\gamma^{(4-2D)n}}, \quad (10)$$

$$F(\tau) = E\{[h(x + \tau) - h(x)]^2\} = 2[R_h(0) - R_h(\tau)], \quad (11)$$

where $R_h(\tau)$ represents the ACF of $h(x)$. According to the Wiener-Khinchin theorem, the exact form of Eq. (11) can be obtained using the inverse Fourier transform of power

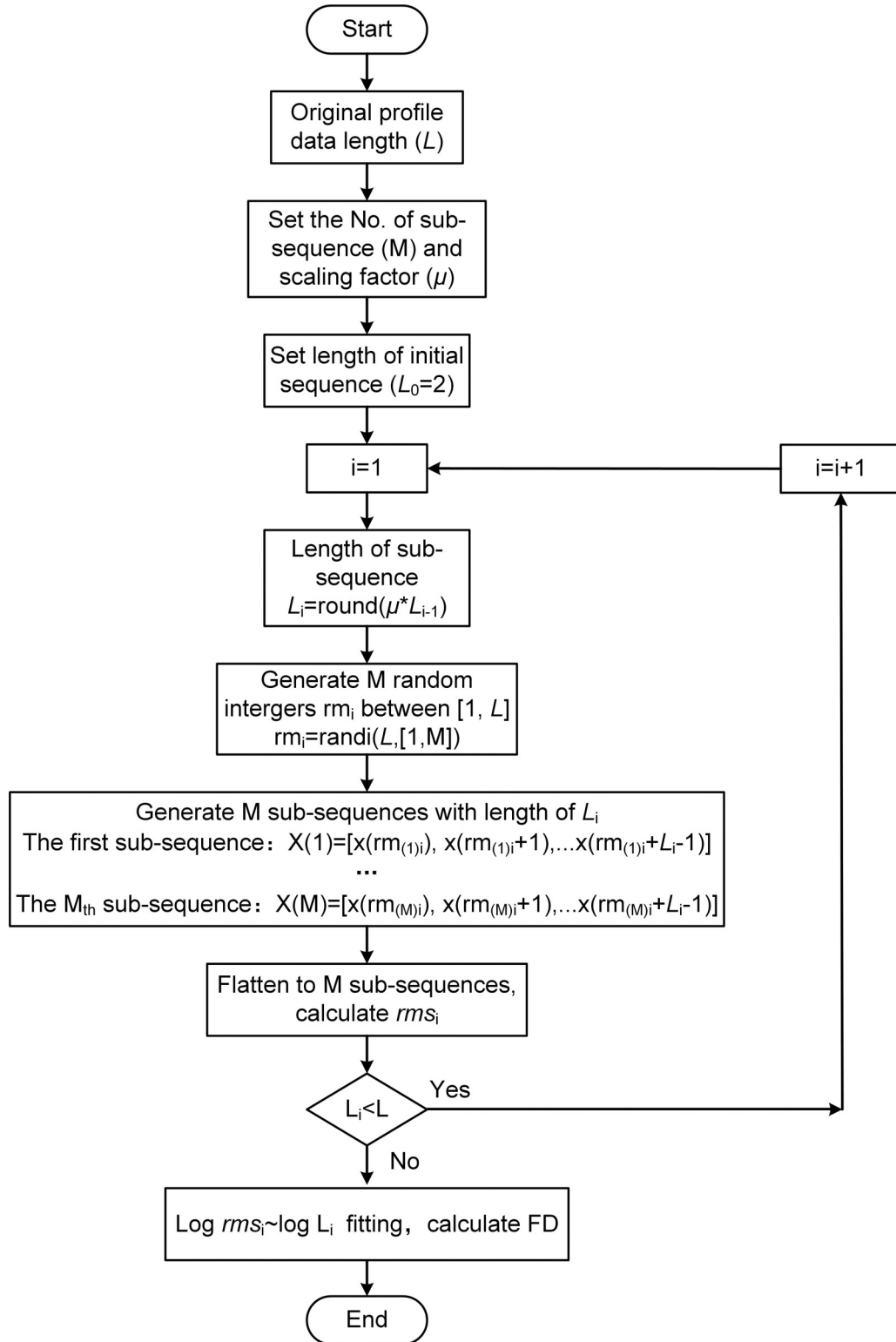


FIG. 2. Flowchart of the RSE method to calculate fractal dimension.

spectrum:

$$F(\tau) \approx \frac{\Gamma(2D - 3)}{(4 - 2D) \ln \gamma} \tau^{(4-2D)}, \quad (12)$$

where Γ represents Gamma function. From Eq. (12) it can be learned that if the value of D is deterministic, $F(\tau) \propto \tau^{4-2D}$.

3. Roughness scaling extract

The RSE method was proposed to calculate the value of D through the relationship between the root-mean-square roughness (rms) with different sampling length [18,19]. The exact procedure is shown in Fig. 2.

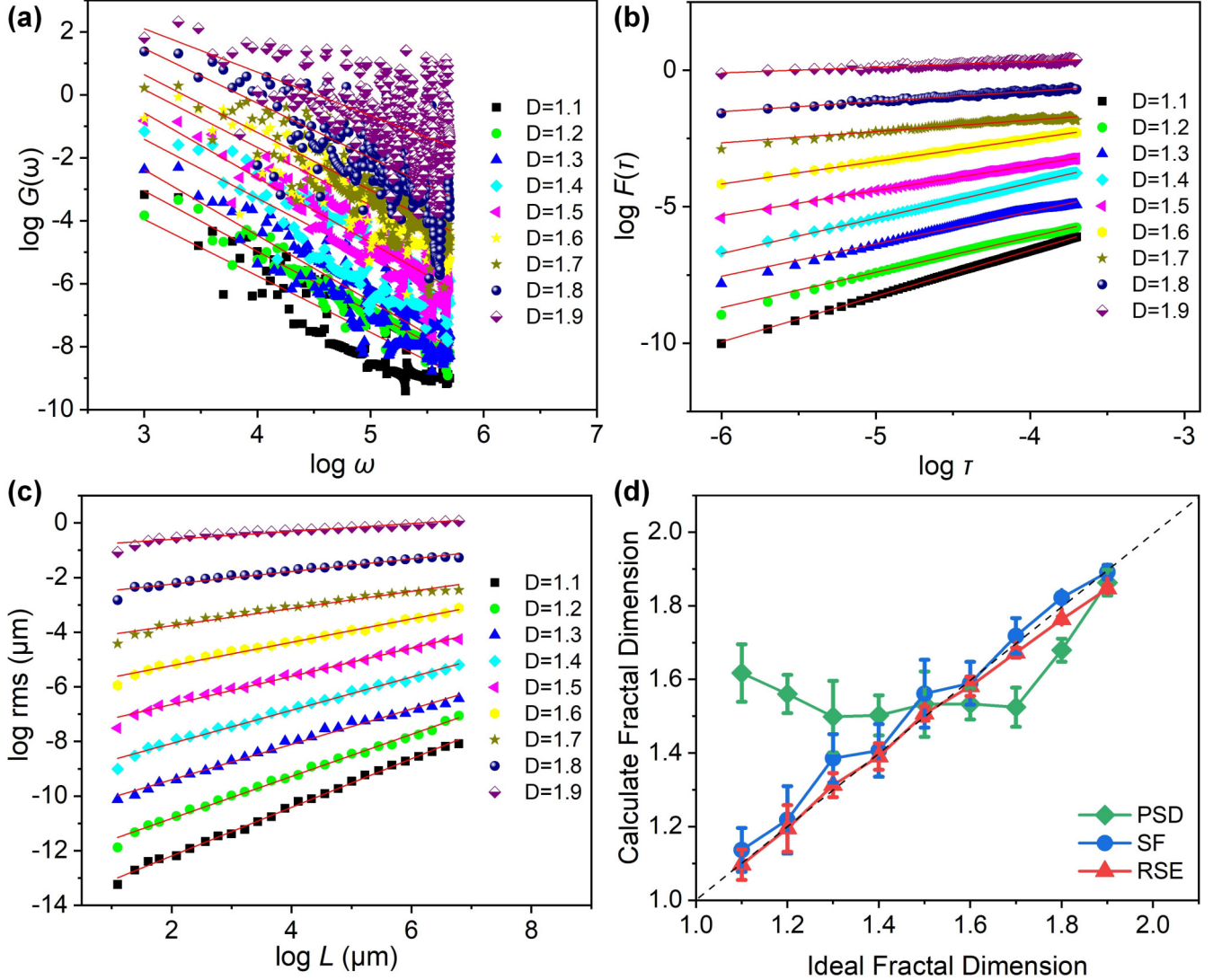


FIG. 3. Fractal-dimension calculation results of artificial 2D contours with the (a) PSD, (b) SF, and (c) RSE methods for fraction value D of 1.1 (black square), 1.2 (green circle), 1.3 (blue upward triangle), 1.4 (cyan diamond), 1.5 (magenta left triangle), 1.6 (yellow star), 1.7 (dark yellow star), 1.8 (navy sphere), 1.9 (purple half-down diamond), and (d) calculation accuracy comparison among PSD (green diamond line), SF (blue circle line) and RSE (red triangle line).

For a data sequence of length L , $X = x(1), x(2), \dots, x(L)$, where $x(n)$ is the n th data point. Then, the subsequence number M and the scaling factor μ are selected. The length of the subsequence L_i is determined by the initial subsequence length L_0 and scaling factor μ . After generating M subsequences of length L_i , the flattening is performed. Specifically, the flattening process is original subsequence, subtracting the fitting results with orders of 0, 1, and 2. In this study, 1-order fitting was selected. According to the study of Wang [32], M and μ were set to 50 and 0.85, respectively.

Because rms is equal to the square root of the variance, the relationship between rms and frequency can be obtained from Eqs. (13) and (14):

$$\text{rms} = \sqrt{E[(h(x) - E[h(x)])^2]} = \sqrt{E[h^2(x)]}, \quad (13)$$

$$\begin{aligned} \text{rms} &= \sqrt{R_h(\tau)|_{\tau=0}} = \sqrt{\frac{1}{2\pi} \int_{\omega_l}^{\omega_h} G_h(\omega) e^{j\omega\tau} d\omega|_{\tau=0}} \\ &= C \sqrt{|\omega_h^{(2D-4)} - \omega_l^{(2D-4)}|}. \end{aligned} \quad (14)$$

In Eq. (14), $C = \sqrt{\frac{1}{8 \ln \gamma} \frac{1}{D-2}}$. It should be noted that the low-frequency limit ω_l corresponds to the length of the sample, while the high-frequency limit ω_h corresponds to the Nyquist frequency, which is related to the resolution of the instrument [20].

C. Rabinovich fractal model

Rumpf's theory proposes a method for calculating the van der Waals force between a sphere and a rough surface [33].

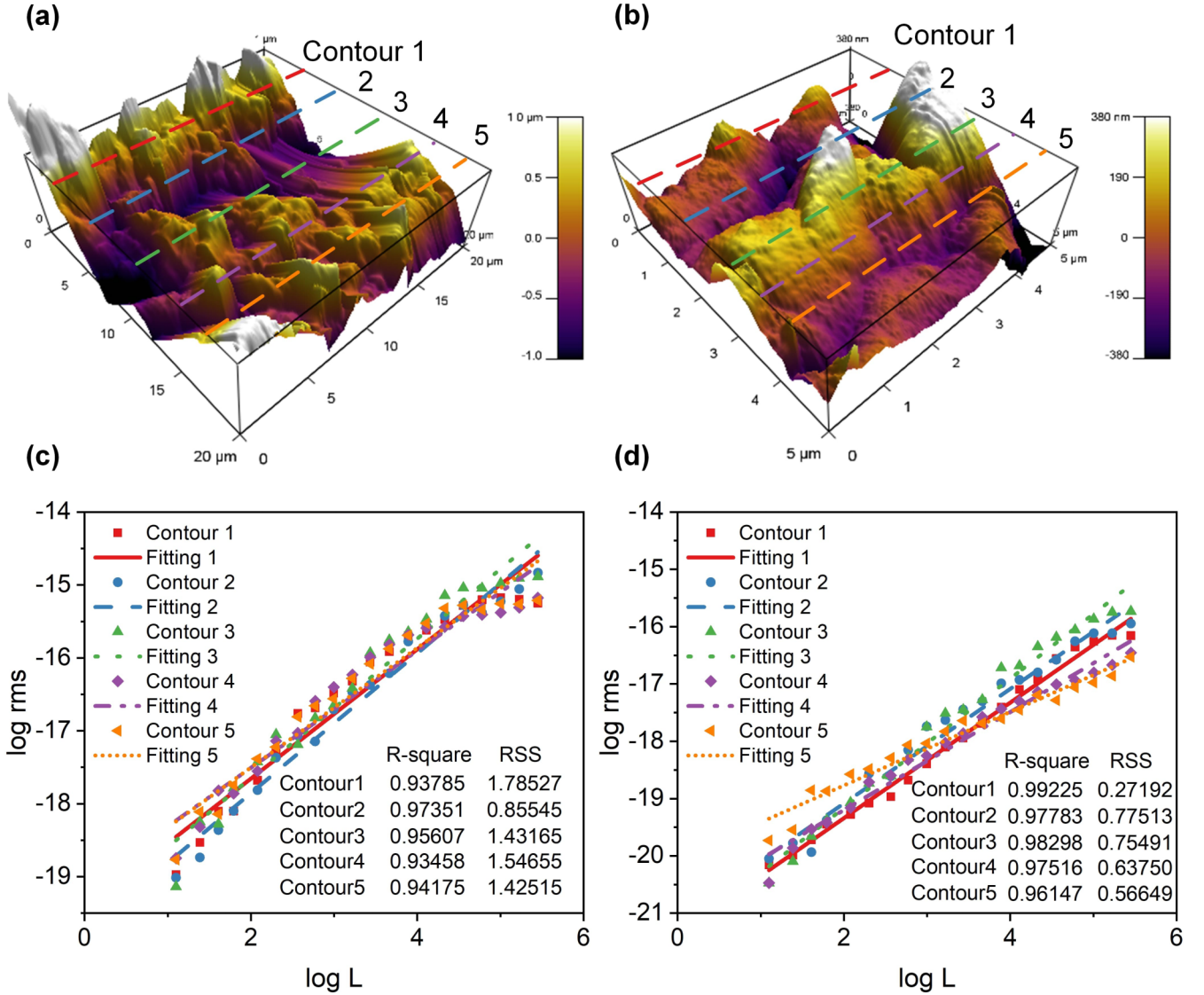


FIG. 4. Morphology of etched-Al surface in the area of (a) $20 \times 20 \mu\text{m}^2$, (b) $5 \times 5 \mu\text{m}^2$, and (c) RSE fitting results of (a), and (d) RSE fitting results of (b); the fitting lines correspond to contours 1–5 are solid, dashed, dotted, dashed-dotted-dotted, and short dotted, respectively.

Rabinovich improved the model to obtain a formula for calculating the adhesion force [24,25]:

$$F_{\text{ad}} = \frac{AR}{6H_0^2} \left[\frac{1}{1 + R/(1.48 \text{ rms})} + \frac{1}{(1 + 1.48 \text{ rms}/H_0)^2} \right], \quad (15)$$

where A is the Hamaker constant, R is the radius of the sphere, and H_0 is the balance distance. If the surface is a fractal surface, Eq. (15) can be introduced to replace rms with Eq. (14). Thus, a method for calculating adhesion force can be obtained:

$$F_{\text{ad}} = \frac{AR}{6H_0^2} \left[\frac{1}{1 + R/(1.48C\sqrt{\omega_h^{2D-4} - \omega_l^{2D-4}})} + \frac{1}{(1 + 1.48C\sqrt{\omega_h^{2D-4} - \omega_l^{2D-4}}/H_0)^2} \right]. \quad (16)$$

When $\omega_h \gg \omega_l$, Eq. (16) can be simplified as Eq. (17):

$$F_{\text{ad}} = \frac{AR}{6H_0^2} \left[\frac{1}{1 + R/(1.48C\omega_h^{D-2})} + \frac{1}{(1 + 1.48C\omega_h^{D-2}/H_0)^2} \right], \quad (17)$$

For convenience, Eq. (17) is referred to as the RF model.

III. RESULTS

A. Artificial surface analysis with different methods

The D_c results obtained using the PSD, SF, and RSE methods for the contours in Fig. 1 are shown in Figs. 3(a)–3(c), respectively.

From Fig. 3(a), the accuracy of the traditional PSD method is limited, and accurate calculation cannot be realized when the theoretical fractal dimension is too large or too small.

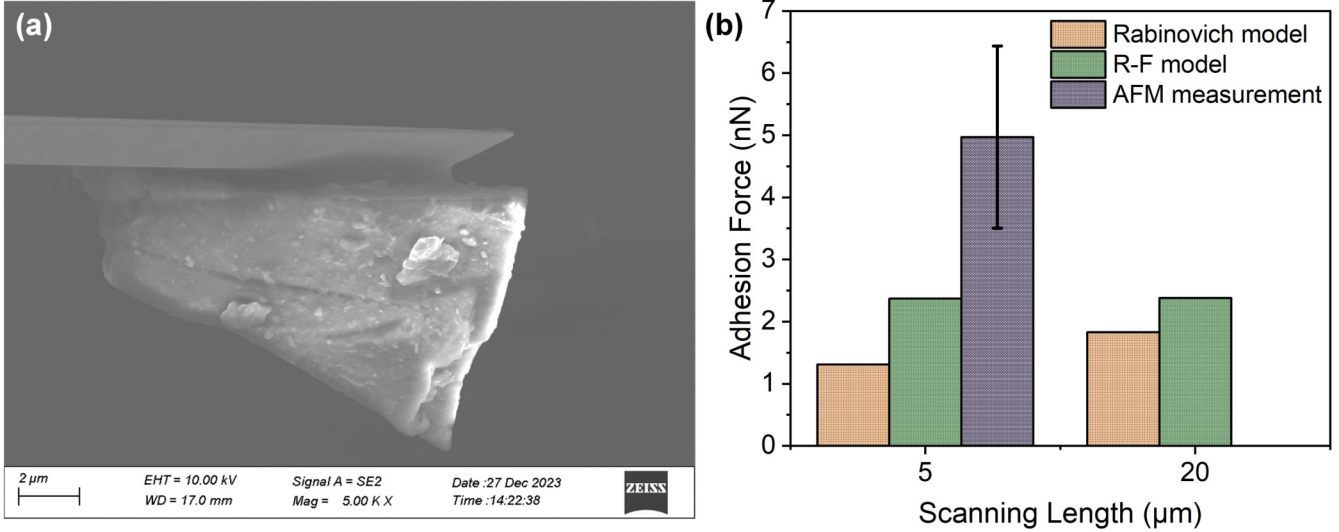


FIG. 5. AFM adhesion test between (a) the lab-made tip and the etched surface, and (b) comparison of the calculation results (Rabinovich-model fill pattern with dotted grid, and RF-model fill pattern with wave) with the AFM adhesion result (fill pattern with horizontal brick).

However, the SF and RSE methods have higher calculation accuracy and can be realized in the full range of theoretical fractal dimensions. To show the accuracy of the calculation methods more clearly, five sets of 2D contours of the full range of D_i similar to Fig. 2 were generated using $h(x)$, and then the D_c were calculated using different methods; the corresponding relative calculation errors of the three methods are shown in Fig. 3(d).

The dashed black line in Fig. 3(d) has a slope of 1, indicating an accuracy of 100%. The fractal dimension calculated using the RSE method was closest to the ideal fractal dimension. For values of D_i less than 1.7, the red line (RSE method) almost coincides with the dashed black line. When D_i is greater than 1.7, the calculated results are small compared with the D_i , owing to the nature of the RSE method. The reason for this result is that when D_i is too large, the RSE method may eliminate some details during the flattening operation, thereby affected the accuracy of the calculated results. The average relative error of the three methods calculated using $|D_c - D_i|/D_i$ were 13.88, 2.16, and 1.17% for the PSD, SF and RSE methods, respectively, indicating that the contour fractal dimensions can be evaluated most efficiently using the RSE method.

B. Real surface analysis with RSE method

An etched-Al surface was used to clarify the accuracy of the RSE method and apply the calculation results to the fractional contact theory. From this approach, the adhesion force on the basis of fractal theory can be obtained. As shown in Fig. 4, the topography of Al surface was measured using AFM. Five contours were extracted from each image, and the average D was calculated using the RSE method. The D_c calculated from 20 μm was 1.157 and that from 5 μm was 1.074, which is attributed to the morphology of fine asperities and voids which could be recognized in AFM images with L smaller than 10 μm [19].

C. Adhesion force measurement and calculation

Once the fractal dimension D of the true contour is obtained, the adhesion force can be calculated using Eq. (16), which shows that the adhesion force depends on the value of D and the number of sampling points N . When N is bigger, more details of the morphology are captured, and then the D_c results are affected, similar to the result of Ref. [34].

To compare with actual measurement results, a lab-made AFM tip [Fig. 5(a)] was used in the contact force mode to measure the adhesion force between the tip and the etched surface; details of the AFM tip fabrication can be found in our previous research [30]. As shown in Fig. 5(b), the measured value was much larger than the calculated value, which is attributed to the composition of the adhesion force. The AFM adhesion force is composed of van der Waals-, electrostatic-, and capillary forces. According to the electrostatic force calculation method of Zhang [35], the total electrostatic force F_E can be written as shown in the following equation, where the electric field force F_e is 0:

$$F_E = F_{es} + F_{el} + F_e = \frac{Q_{dust}^2}{16\pi\epsilon_0(h+z)^2} + \frac{\pi\epsilon_0RU_e^2}{2z}. \quad (17)$$

The particle charge, Q_{dust} , is 1.6473×10^{-20} C. The equivalent particle charge position, h , is approximately $R/2$, where R is the tip curvature radius of 0.3 μm. The permittivity, ϵ_0 , is 8.8541×10^{-12} F/m. The contact potential difference, U_e , is 0 ~ 0.5 V. The distance between the tip and the etched surface, z , is typically 0.40 nm.

The capillary force was calculated using the method proposed by Willet [36]. More specifically, the tip particle and etched surface were considered as two spheres, which can be expressed by

$$F_C = 2\pi r_N \zeta - \pi r_N^2 \Delta P - V_s \rho g. \quad (18)$$

The surface tension of water, ζ , is 7.28×10^{-2} N/m. The density of water, ρ , is 1 g/cm³. The radius of the capillary

bridge neck, r_N , is equal to $R/30$. ΔP is the hydrostatic pressure difference across the air-liquid interface, equal to ζ/r' , where r' is the curvature radius of the liquid bridge, equal to $30R$. V_s is the volume of the tip particle, $5.6549 \times 10^{-20} \text{ m}^3$, and g is the gravitational acceleration.

Once the electrostatic and capillary forces have been calculated, the true van der Waals force from the AFM adhesion test can be obtained by subtracting these two forces from the total adhesion force. The electrostatic force F_E was 2.61 nN and the capillary force F_c was 4.57 nN, which is close to the results of Jang [37]. Therefore, the true van der Waals force was 3.8 nN, which was closer to the RF model result (2.38 nN). This analysis shows that the RF model calculation results are consistent with the experimental results with good accuracy. Moreover, the RF model shows the scale-invariant properties, i.e., the van der Waals calculation results were consistent with sampling lengths at different length scales. In contrast, the original Rabinovich model is sensitive to the sampling length (1.31 nN at the length of 5 μm , and 1.83 nN at the length of 20 μm), which is attributed to the scale-dependent parameter rms.

IV. CONCLUSION

In this study, a more reasonable WM function is proposed to simulate true 2D contours. This WM function $h(x)$ has a simplified form and satisfies random properties, whose expectation and ACF elucidate its reasonable use in spectrum analysis. In addition, the traditional fractal-dimension calculation method and the RSE method were compared to assess the calculation accuracy, showing that the RSE method is an excellent way to calculate the D_c of the contour. Subsequently, the fractal parameter D was introduced into the Rabinovich model to calculate the van der Waals force between a dust particle and surfaces. From the calculation and AFM adhesion test results, we found that the RF model result is closer to the experimental result and clearly does not depend on the sampling length, which is attributed to the fact that rms is not a scale-invariant parameter. Thus, our proposed method to calculate the van der Waals force between two solids, based on the fractal theory, is scale independent and may have potential applications in contact mechanics.

Data will be made available on request.

ACKNOWLEDGMENTS

This work is sponsored by the National Key Research and Development Program (Grant No. 2022YFB3204800), the National Natural Science Foundation of China (Grant No. 52375573), the Youth Innovation Team of Shaanxi Universities (Grant No. 2022–63), and the Fundamental Research Funds for the Central Universities (Grant No. ZYTS24032).

X.W. contributed to conceptualization of the proposed model, designing for the methodology, and writing of computational scripts and the main manuscript; W.W. contributed to project administration, funding acquisition, and grammar checking of the manuscript; Y.Z. contributed to methodology of the computational model. H.Z. did some experimental validation of the proposed model; J.Z. did validation and grammar revision of the manuscript; and Y.L. helped with methodology and validation of the proposed model.

The authors declare no conflicts of interest for this work.

APPENDIX

1. *In situ* observation of dynamic contact

An *in situ* SEM system was used to observe the dynamic contact process. The tip used in this system corresponds to that used in the AFM adhesion test [Fig. 5(a)]. The particle adhered to the cantilever exhibited strong adhesion characteristic, enabling clearer observation of the adhesion process. Before the tip approached the surface, the cantilever remained horizontal, and as the gap between the tip and surface decreased, the cantilever started to bend until they came in contact with each other. Even if the contact region is small, it can be considered two semispherical contacts after magnification, which is expressed in the Rabinovich model. In contrast, when the tip is far away from the surface, the situation is the opposite. With the gap gradually increasing, the cantilever bends up to a certain point. It was noted that at this point the cantilever suddenly detaches from the surface, which corresponds to the “pull-off force” on the AFM adhesion test (the details of dynamic contact process can be found in Supplemental Material Video S1 [38]). Regardless of whether the contact spots are small, the contact region can be simplified as a geometric model. It is necessary to use a scale-independent theory to analyze the contact process, because a magnification system such as SEM is not always available for characterization.

2. The method for obtaining the expectation values

a. Equation (3):

$$\begin{aligned}
 E[Z(x)] &= E \left[\lim_{n \rightarrow \infty} \sum_{i=-n}^n \frac{\cos \phi_i - \cos(\gamma^i x + \phi_i)}{\gamma^{(2-D)i}} \right] \\
 &= \lim_{n \rightarrow \infty} E \left[\sum_{i=-n}^n \frac{\cos \phi_i - \cos(\gamma^i x + \phi_i)}{\gamma^{(2-D)i}} \right] \\
 &= \lim_{n \rightarrow \infty} \underbrace{\int_0^{2\pi} \cdots \int_0^{2\pi}}_{2n+1} \sum_{i=-n}^n \frac{\cos \phi_i - \cos(\gamma^i x + \phi_i)}{\gamma^{(2-D)i}} f_{\Phi}(\phi_i) d\phi_{-1} d\phi_{-2} \cdots d\phi_{-n} d\phi_0 d\phi_1 d\phi_2 \cdots d\phi_n, \quad (\text{A1})
 \end{aligned}$$

where $f_\Phi(\phi_i)$ is the probability density function of ϕ_i . Because of $\phi_n \sim U(0, 2\pi)$, $f_\Phi(\phi_i) = f_\Phi(\phi) = \frac{1}{2\pi}$, and Eq. (A1) can be written as

$$\begin{aligned}
E[Z(x)] &= \lim_{n \rightarrow \infty} \underbrace{\int_0^{2\pi} \cdots \int_0^{2\pi}}_{2n+1} \sum_{i=-n}^n \frac{\cos \phi_i - \cos(\phi_i + \gamma^i x)}{\gamma^{(2-D)i}} f_\Phi^{2n+1}(\phi) d\phi_{-1} d\phi_{-2} \cdots d\phi_{-n} d\phi_0 d\phi_1 d\phi_2 \cdots d\phi_n \\
&= \lim_{n \rightarrow \infty} \underbrace{\int_0^{2\pi} \cdots \int_0^{2\pi}}_{2n+1} \left(\frac{1}{2\pi}\right)^{2n+1} \sum_{i=-n}^n \frac{\cos \phi_i - \cos(\phi_i + \gamma^i x)}{\gamma^{(2-D)i}} d\phi_{-1} d\phi_{-2} \cdots d\phi_{-n} d\phi_0 d\phi_1 d\phi_2 \cdots d\phi_n \\
&= \lim_{n \rightarrow \infty} \underbrace{\int_0^{2\pi} \cdots \int_0^{2\pi}}_n \left(\frac{1}{2\pi}\right)^n \sum_{i=1}^n \frac{\cos \phi_i - \cos(\phi_i + \gamma^i x)}{\gamma^{(2-D)i}} d\phi_1 d\phi_2 d\phi_3 \cdots d\phi_n \\
&= \lim_{n \rightarrow \infty} \underbrace{\int_0^{2\pi} \cdots \int_0^{2\pi}}_{n-1} \left(\frac{1}{2\pi}\right)^{n-1} \sum_{i=2}^n \frac{\cos \phi_i - \cos(\phi_i + \gamma^i x)}{\gamma^{(2-D)i}} d\phi_2 d\phi_3 \cdots d\phi_n \\
&= \lim_{n \rightarrow \infty} \int_0^{2\pi} \frac{1}{2\pi} \frac{\cos \phi_n - \cos(\phi_n + \gamma^n x)}{\gamma^{(2-D)n}} d\phi_n = 0.
\end{aligned} \tag{A2}$$

b. Equation (4):

$$\begin{aligned}
&E[Z(x + \tau)Z(x)] \\
&= E \left[\sum_{m=-\infty}^{\infty} \sum_{n=-\infty}^{\infty} \frac{\cos \phi_n - \cos[\gamma^n(x + \tau) + \phi_n]}{\gamma^{(2-D)n}} \frac{\cos \phi_m - \cos(\gamma^m x + \phi_m)}{\gamma^{(2-D)m}} \right] \\
&= E \left[\lim_{m \rightarrow \infty} \lim_{n \rightarrow \infty} \sum_{k=-m}^m \sum_{l=-n}^n \frac{\cos \phi_l - \cos[\gamma^l(x + \tau) + \phi_l]}{\gamma^{(2-D)l}} \frac{\cos \phi_k - \cos(\gamma^k x + \phi_k)}{\gamma^{(2-D)k}} \right] \\
&= \lim_{m \rightarrow \infty} \lim_{n \rightarrow \infty} E \left[\sum_{k=-m}^m \sum_{l=-n}^n \frac{[\cos \phi_l - \cos(\gamma^l(x + \tau) + \phi_l)][\cos \phi_k - \cos(\gamma^k x + \phi_k)]}{\gamma^{(2-D)(l+k)}} \right] \\
&= \lim_{m \rightarrow \infty} \lim_{n \rightarrow \infty} \sum_{k=-m}^m \sum_{l=-n}^n E \left[\frac{[\cos \phi_l \cos \phi_k - \cos \phi_l \cos(\gamma^k x + \phi_k) - \cos \phi_k \cos[(\gamma^l(x + \tau) + \phi_l)] + [\cos(\gamma^l(x + \tau) + \phi_l) \cos(\gamma^k x + \phi_k)]]}{\gamma^{(2-D)(l+k)}} \right] \\
&= \lim_{m \rightarrow \infty} \lim_{n \rightarrow \infty} \sum_{k=-m}^m \sum_{l=-n}^n E \left[\frac{\cos(\phi_l + \phi_k) + \cos(\phi_l - \phi_k) - \cos(\phi_l + \gamma^k x + \phi_k) - \cos(\phi_l - \phi_k - \gamma^k x) - \cos[\phi_k + \phi_l + \gamma^l(x + \tau)] - \cos[\phi_k - \phi_l - \gamma^l(x + \tau)] + \cos[\phi_k + \phi_l + \gamma^l(x + \tau) + \gamma^k x] + \cos[\phi_l - \phi_k + \gamma^l(x + \tau) - \gamma^k x]}{2\gamma^{(2-D)(l+k)}} \right]
\end{aligned} \tag{A3}$$

$$E[\cos(\phi_l + \phi_k)] = \int_0^{2\pi} \int_0^{2\pi} \cos(\phi_l + \phi_k) \left(\frac{1}{2\pi}\right)^2 d\phi_l d\phi_k = 0$$

$$E[\cos(\phi_l - \phi_k)] = \int_0^{2\pi} \int_0^{2\pi} \cos(\phi_l - \phi_k) \left(\frac{1}{2\pi}\right)^2 d\phi_l d\phi_k = \begin{cases} 0, & l \neq k \\ 1, & l = k \end{cases}$$

$$E[\cos(\phi_l + \gamma^k x + \phi_k)] = \int_0^{2\pi} \int_0^{2\pi} \cos(\phi_l + \gamma^k x + \phi_k) \left(\frac{1}{2\pi}\right)^2 d\phi_l d\phi_k = 0$$

$$E[\cos(\phi_l - \phi_k - \gamma^k x)] = \int_0^{2\pi} \int_0^{2\pi} \cos(\phi_l - \phi_k - \gamma^k x) \left(\frac{1}{2\pi}\right)^2 d\phi_l d\phi_k = \begin{cases} 0, & l \neq k \\ \cos \gamma^k x, & l = k \end{cases}$$

$$\begin{aligned}
E[\cos(\phi_k + \phi_l + \gamma^l(x + \tau))] &= \int_0^{2\pi} \int_0^{2\pi} \cos(\phi_k + \phi_l + \gamma^l(x + \tau)) \left(\frac{1}{2\pi}\right)^2 d\phi_l d\phi_k = 0 \\
E[\cos(\phi_k - \phi_l - \gamma^l(x + \tau))] &= \int_0^{2\pi} \int_0^{2\pi} \cos[\phi_k - \phi_l - \gamma^l(x + \tau)] \left(\frac{1}{2\pi}\right)^2 d\phi_l d\phi_k = \begin{cases} 0, & l \neq k \\ \cos \gamma^k(x + \tau), & l = k \end{cases} \\
E[\cos(\phi_k + \phi_l + \gamma^l(x + \tau) + \gamma^k x)] &= \int_0^{2\pi} \int_0^{2\pi} \cos[\phi_k + \phi_l + \gamma^l(x + \tau) + \gamma^k x] \left(\frac{1}{2\pi}\right)^2 d\phi_l d\phi_k = 0 \\
E[\cos(\phi_l - \phi_k + \gamma^l(x + \tau) - \gamma^k x)] &= \int_0^{2\pi} \int_0^{2\pi} \cos[\phi_l - \phi_k + \gamma^l(x + \tau) - \gamma^k x] \left(\frac{1}{2\pi}\right)^2 d\phi_l d\phi_k = \begin{cases} 0, & l \neq k \\ \cos \gamma^k \tau, & l = k \end{cases} \quad (\text{A4})
\end{aligned}$$

Only $l = k$; Eq. (A3) is not 0. Substituting Eq. (A4) into Eq. (A3), which can be simplified as Eq. (4),

$$E[Z(x + \tau)Z(x)] = \sum_{n=-\infty}^{\infty} \frac{1 + \cos \gamma^n \tau - \cos \gamma^n x - \cos \gamma^n (\tau + x)}{2\gamma^{(4-2D)n}}.$$

c. Equation (6):

$$\begin{aligned}
E[h(x)] &= E\left[\lim_{n \rightarrow \infty} \sum_{i=-n}^n \frac{\cos(\gamma^i x + \phi_i)}{\gamma^{(2-D)i}}\right] = \lim_{n \rightarrow \infty} E\left[\sum_{i=-n}^n \frac{\cos(\gamma^i x + \phi_i)}{\gamma^{(2-D)i}}\right] \\
&= \lim_{n \rightarrow \infty} \underbrace{\int_0^{2\pi} \cdots \int_0^{2\pi}}_{2n+1} \sum_{i=-n}^n \frac{\cos(\gamma^i x + \phi_i)}{\gamma^{(2-D)i}} f_{\Phi}(\phi_i) d\phi_{-1} d\phi_{-2} \cdots d\phi_{-n} d\phi_0 d\phi_1 d\phi_2 \cdots d\phi_n \\
&= \lim_{n \rightarrow \infty} \int_0^{2\pi} \frac{1}{2\pi} \frac{\cos(\phi_n + \gamma^n x)}{\gamma^{(2-D)n}} d\phi_n = 0 \quad (\text{A5})
\end{aligned}$$

d. Equation (7):

$$\begin{aligned}
E[h(x + \tau)h(x)] &= E\left[\sum_{m=-\infty}^{\infty} \sum_{n=-\infty}^{\infty} \frac{\cos[\gamma^m(x + \tau) + \phi_m] \cos(\gamma^n x + \phi_n)}{\gamma^{(2-D)m} \gamma^{(2-D)n}}\right] \\
&= E\left[\lim_{m \rightarrow \infty} \lim_{n \rightarrow \infty} \sum_{k=-m}^m \sum_{l=-n}^n \frac{\cos[\gamma^l(x + \tau) + \phi_l] \cos(\gamma^k x + \phi_k)}{\gamma^{(2-D)l} \gamma^{(2-D)k}}\right] \\
&= \lim_{m \rightarrow \infty} \lim_{n \rightarrow \infty} \sum_{k=-m}^m \sum_{l=-n}^n E\left[\frac{\cos[\gamma^l(x + \tau) + \phi_l] \cos(\gamma^k x + \phi_k)}{\gamma^{(2-D)(l+k)}}\right] \\
&= \lim_{m \rightarrow \infty} \lim_{n \rightarrow \infty} \sum_{k=-m}^m \sum_{l=-n}^n E\left[\frac{\cos[\gamma^l(x + \tau) + \phi_l + \gamma^k x + \phi_k] + \cos[\gamma^l(x + \tau) + \phi_l - \gamma^k x - \phi_k]}{2\gamma^{(2-D)(l+k)}}\right] \quad (\text{A6})
\end{aligned}$$

$$\begin{aligned}
E[\cos(\gamma^l(x + \tau) + \phi_l + \gamma^k x + \phi_k)] &= \int_0^{2\pi} \int_0^{2\pi} \cos(\gamma^l(x + \tau) + \phi_l + \gamma^k x + \phi_k) \left(\frac{1}{2\pi}\right)^2 d\phi_l d\phi_k = 0 \\
E[\cos(\gamma^l(x + \tau) + \phi_l - \gamma^k x - \phi_k)] &= \int_0^{2\pi} \int_0^{2\pi} \cos(\gamma^l(x + \tau) + \phi_l - \gamma^k x - \phi_k) \left(\frac{1}{2\pi}\right)^2 d\phi_l d\phi_k = \begin{cases} 0, & l \neq k \\ \cos \gamma^k \tau, & l = k \end{cases} \quad (\text{A7})
\end{aligned}$$

Only $l = k$, the Eq. (A6) is not 0. Substituting Eq. (A7) into Eq. (A6), which can be simplified as Eq. (7),

$$E[h(x + \tau)h(x)] = \sum_{n=-\infty}^{\infty} \frac{\cos \gamma^n \tau}{\gamma^{(4-2D)n}}.$$

- [1] P. S. Davids, F. Intravaia, F. S. S. Rosa, and D. A. R. Dalvit, Modal approach to Casimir forces in periodic structures, *Phys. Rev. A* **82**, 062111 (2010).
[2] W. Broer, G. Palasantzas, J. Knoester, and V. B. Svetovoy, Roughness correction to the Casimir force at short separations:

Contact distance and extreme value statistics, *Phys. Rev. B* **85**, 155410 (2012).

- [3] F. A. Burger, R. W. Corkery, S. Y. Buhmann, and J. Fiedler, Comparison of theory and experiments on van der Waals forces in media—A survey, *J. Phys. Chem. C* **124**, 24179 (2020).

- [4] P. Loskill, J. Puthoff, M. Wilkinson, K. Mecke, K. Jacobs, and K. Autumn, Macroscale adhesion of gecko setae reflects nanoscale differences in subsurface composition, *J. Roy. Soc. Interf.* **10**, 20120587 (2013).
- [5] J. Fiedler, K. Berland, J. W. Borchert, R. W. Corkery, A. Einfeld, D. Gelbwaser-Klimovsky, M. M. Greve, B. Holst, K. Jacobs, and M. Krüger, Perspectives on weak interactions in complex materials at different length scales, *Phys. Chem. Chem. Phys.* **25**, 2671 (2023).
- [6] T. Thomas, Defining the microtopography of surfaces in thermal contact, *Wear* **79**, 73 (1982).
- [7] Q. Chen, Y. Wang, J. Zhou, Y. Wu, and H. Song, Research on characterization of anisotropic and isotropic processing surfaces by characteristic roughness, *J. Mater. Process. Technol.* **275**, 116277 (2020).
- [8] B. S. Tatone and G. Grasselli, An investigation of discontinuity roughness scale dependency using high-resolution surface measurements, *Rock Mech. Rock Eng.* **46**, 657 (2013).
- [9] S. Chesters, H. Wen, M. Lundin, and G. Kasper, Fractal-based characterization of surface texture, *Appl. Surf. Sci.* **40**, 185 (1989).
- [10] A. Majumdar and C. Tien, Fractal characterization and simulation of rough surfaces, *Wear* **136**, 313 (1990).
- [11] H. Zhou and H. Xie, Direct estimation of the fractal dimensions of a fracture surface of rock, *Surf. Rev. Lett.* **10**, 751 (2003).
- [12] T. Ai, R. Zhang, H. Zhou, and J. Pei, Box-counting methods to directly estimate the fractal dimension of a rock surface, *Appl. Surf. Sci.* **314**, 610 (2014).
- [13] L. S. Liebovitch and T. Toth, A fast algorithm to determine fractal dimensions by box counting, *Phys. Lett. A* **141**, 386 (1989).
- [14] X. Gou and J. Schwartz, Fractal analysis of the role of the rough interface between $\text{Bi}_2\text{Sr}_2\text{CaCu}_2\text{O}_x$ filaments and the Ag matrix in the mechanical behavior of composite round wires, *Supercond. Sci. Technol.* **26**, 055016 (2013).
- [15] C. A. Valentim, C. M. C. Inacio Jr., and S. A. David, Fractal methods and power spectral density as means to explore EEG patterns in patients undertaking mental tasks, *Fractal Fract.* **5**, 225 (2021).
- [16] J.-J. Wu, Structure function and spectral density of fractal profiles, *Chaos Solitons Fractals* **12**, 2481 (2001).
- [17] R. Sayles and T. Thomas, The spatial representation of surface roughness by means of the structure function: A practical alternative to correlation, *Wear* **42**, 263 (1977).
- [18] F. Feng, J. Huang, X. Li, T. Qu, B. Liu, W. Zhou, X. Qian, and P. Feng, Influences of planarization modification and morphological filtering by AFM probe-tip on the evaluation accuracy of fractal dimension, *Surf. Coat. Technol.* **363**, 436 (2019).
- [19] F. Feng, B. Liu, X. Zhang, X. Qian, X. Li, J. Huang, T. Qu, and P. Feng, Roughness scaling extraction method for fractal dimension evaluation based on a single morphological image, *Appl. Surf. Sci.* **458**, 489 (2018).
- [20] A. Majumdar and B. Bhushan, Role of fractal geometry in roughness characterization and contact mechanics of surfaces, *J. Tribol.* **112**, 205 (1990).
- [21] A. Majumdar and B. Bhushan, Fractal model of elastic-plastic contact between rough surfaces, *J. Tribol.* **113**, 1 (1991).
- [22] J. A. Greenwood and J. P. Williamson, Contact of nominally flat surfaces, *Proc. R. Soc. London Ser. A* **295**, 300 (1966).
- [23] J. A. Greenwood and J. H. Tripp, The elastic contact of rough spheres, *J. Appl. Mech.* **34**, 153 (1967).
- [24] Y. I. Rabinovich, J. J. Adler, A. Ata, R. K. Singh, and B. M. Moudgil, Adhesion between nanoscale rough surfaces: I. Role of asperity geometry, *J. Colloid Interface Sci.* **232**, 10 (2000).
- [25] Y. I. Rabinovich, J. J. Adler, A. Ata, R. K. Singh, and B. M. Moudgil, Adhesion between nanoscale rough surfaces: II. Measurement and comparison with theory, *J. Colloid Interface Sci.* **232**, 17 (2000).
- [26] H. Ding, C. Shi, L. Ma, Z. Yang, M. Wang, Y. Wang, T. Chen, L. Sun, and F. Toshio, Visual servoing-based nanorobotic system for automated electrical characterization of nanotubes inside SEM, *Sensors* **18**, 1137 (2018).
- [27] Q. Shi, Z. Yang, Y. Guo, H. Wang, L. Sun, Q. Huang, and T. Fukuda, A vision-based automated manipulation system for the pick-up of carbon nanotubes, *IEEE/ASME Trans. Mechatron.* **22**, 845 (2017).
- [28] M. V. Berry, Z. Lewis, and J. F. Nye, On the Weierstrass-Mandelbrot fractal function, *Proc. R. Soc. London Ser. A* **370**, 459 (1980).
- [29] R. S. Sayles and T. R. Thomas, Surface topography as a nonstationary random process, *Nature (London)* **271**, 431 (1978).
- [30] X. Wang, W. Wang, H. Shao, S. Chao, H. Zhang, C. Tang, X. Li, Y. Zhu, J. Zhang, and X. Zhang, Lunar dust-mitigation behavior of aluminum surfaces with multiscale roughness prepared by a composite etching method, *ACS Appl. Mater. Interf.* **14**, 34020 (2022).
- [31] L. Cohen, The generalization of the Wiener-Khinchin theorem, in *Proceedings of the 1998 IEEE International Conference on Acoustics, Speech and Signal Processing, ICASSP'98* (Cat. No. 98CH36181) (IEEE, Seattle, 1998), pp. 1577–1580.
- [32] S. Wang, J. Zhang, F. Feng, X. Qian, L. Jiang, J. Huang, B. Liu, J. Li, Y. Xia, and P. Feng, Fractal analysis on artificial profiles and electroencephalography signals by roughness scaling extraction algorithm, *IEEE Access* **7**, 89265 (2019).
- [33] H. Rumpf, *Particle Technology* (Springer Science & Business Media, Berlin, 2012).
- [34] M. Nasehnejad, G. Nabiyouni, and M. G. Shahraki, Fractal analysis of nanostructured silver film surface, *Chin. J. Phys.* **55**, 2484 (2017).
- [35] H. Zhang, X. Wang, J. Zhang, M. Mu, M. Wang, Y. Zhu, and W. Wang, Adhesion effect analysis of ultra-fine lunar dust particles on the aluminum-based rough surface based on the fractal theory, *Adv. Space Res.* **69**, 2745 (2022).
- [36] C. D. Willett, M. J. Adams, S. A. Johnson, and J. P. Seville, Capillary bridges between two spherical bodies, *Langmuir* **16**, 9396 (2000).
- [37] J. Jang, G. C. Schatz, and M. A. Ratner, Capillary force in atomic force microscopy, *J. Chem. Phys.* **120**, 1157 (2004).
- [38] See Supplemental Material at <http://link.aps.org/supplemental/10.1103/PhysRevE.110.034802> for the details of dynamic contact process between the dust particle and the rough surface.